Comparative First-Principles Study of Antiperovskite Oxides and Nitrides as Thermoelectric Material: Multiple Dirac Cones, Low-Dimensional Band Dispersion, and High Valley Degeneracy

Masayuki Ochi* and Kazuhiko Kuroki
Department of Physics, Osaka University, Machikaneyama-cho, Toyonaka, Osaka 560-0043, Japan

(Received 9 February 2019; revised manuscript received 9 August 2019; published 6 September 2019)

We perform a comparative study on thermoelectric performance of antiperovskite oxides Ae_3TtO and nitrides Ae_3PnN ($Ae = \mathrm{Ca, Sr, Ba}$; $Tt = \mathrm{Ge, Sn, Pb}$; $Pn = \mathrm{As, Sb, Bi}$) by means of first-principles calculation. As for the oxides with the cubic structure, Ca_3GeO with a sizable band gap exhibits high thermoelectric performance at high temperatures, while Ba_3PbO with Dirac cones without the gap is favorable at low temperatures. The latter high performance owes to high valley degeneracy, including the multiple Dirac cones and the valleys near the Γ and R points. For the nitrides with the cubic structure, an insulator with strong quasi-one-dimensionality exhibits high thermoelectric performance. We also find that the orthorhombic structural distortion sometimes sizably enhances thermoelectric performance, especially for Ba_3GeO and Sr_3AsN, where the high valley degeneracy is realized in the *Pnma* phase. Our calculation reveals that antiperovskites offer a fertile playground of various kinds of characteristic electronic structures, which enhance thermoelectric performance, and provide promising candidates for high-performance thermoelectric materials.

DOI: 10.1103/PhysRevApplied.12.034009

I. INTRODUCTION

Searching for high-performance thermoelectric materials is a central issue in the study of themoelectrics. There are many promising compounds such as Bi_2Te_3 [1–3], lead chalcogenides [4–7], skutterudites [8–12], clathrates [13], and Na_xCoO_2 [14]. These high-performance materials have some characteristics in their crystal and/or electronic structures. For example, the rattling motion of atoms is key for the low thermal conductivity in skutterudites and clathrates [13,15–24]. Band convergence studied in lead chalcogenides [25] is one of the most important and general concepts to enhance thermoelectric performance. Low dimensionality [26–29] is also an important concept for enhancing the thermoelectric performance of many materials, including layered materials, nanowires, and nanotubes [30–32]. It was pointed out that the high thermoelectric performance of Na_xCoO_2 originates from a pudding-mold-shaped band structure [33], where a large group velocity and a high density of states (DOS) can coexist. These studies show that investigating characteristic crystal and/or electronic structures often results in general and useful concepts for seeking high thermoelectric performance.

Antiperovskites, in which the positions of constituent elements in a famous perovskite structure are interchanged as shown in Fig. 1(a), have attracted much attention from several aspects, such assuperconductivity [35,36], giant negative thermal expansion [37,38], giant magnetoresistance [39], magnetostriction [40], and magnetocaloric effects [41]. Interestingly, recent studies have also pointed out that some antiperovskite oxides and nitrides are candidates for three-dimensional massless Dirac electron systems [42–44] and topological crystalline insulators [45]. They also belong to mixed-anion compounds [46], which are characterized by multiple anion atoms. For example, Sr_3SnO has two kinds of anion atoms, O^{2-} and Sn^{4-}, the latter of which is an unusual negative oxidation state of group-14 elements. The unique crystal and electronic structures of antiperovskites have been investigated also as possible candidates for thermoelectric materials in experimental [47] and theoretical [48–60] studies. The experimental realization of the carrier control and a high Seebeck coefficient of around 100 $\mu\mathrm{V\,K^{-1}}$, together with a metallic resistivity and a relatively low thermal conductivity of around 2 $\mathrm{W\,m^{-1}\,K^{-1}}$ at room temperature, is promising [47]. However, it is still unclear whether their characteristic electronic structure including the Dirac dispersion is favorable for thermoelectric performance and how to enhance their performance. Because of their unique characteristics, it is expected that investigation of the thermoelectric properties of antiperovskites will provide novel and important knowledge that will expand the possibility for further findings of high-performance thermoelectric materials.

*ochi@phys.sci.osaka-u.ac.jp

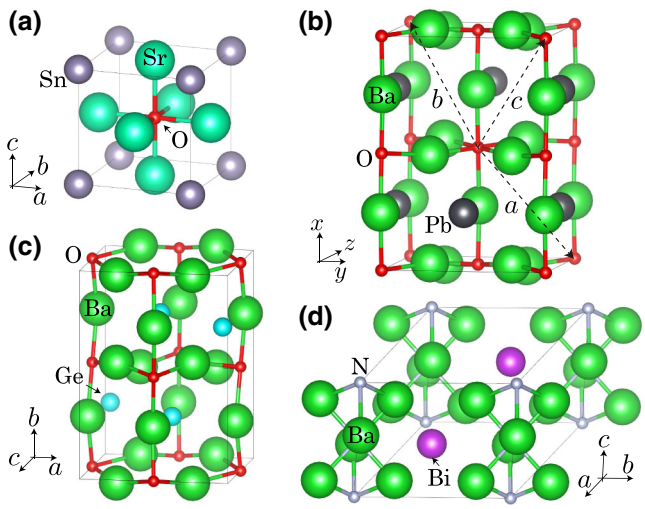

FIG. 1. Crystal structures of (a) Sr_3SnO ($Pm\bar{3}m$), (b) Ba_3PbO ($Imma$), (c) Ba_3GeO ($Pnma$), and (d) Ba_3BiO ($P6_3/mmc$). A doubled unit cell is shown in panel (b), while the lattice vectors a, b, and c for the primitive unit cell are also shown with broken lines. This figure is depicted using VESTA software [34].

In this paper, we perform a comparative study on thermoelectric performance of antiperovskite oxides Ae_3TtO and nitrides Ae_3PnN (Ae = Ca, Sr, Ba; Tt = Ge, Sn, Pb; Pn = As, Sb, Bi) by means of first-principles calculation. We find that several kinds of characteristic electronic structure play an important role in enhancing their thermoelectric performance: multiple Dirac cones, quasi-one-dimensional band dispersion, and high valley degeneracy induced by the structural distortion toward the orthorhombic *Pnma* phase. Here, because the crystal structure of the antiperovskite oxides and nitrides exhibits some variations as presented in Tables I and II, we investigate the effect of the structural change on their thermoelectric performance. Our study reveals a unique and fertile electronic structure of the antiperovskite oxides and nitrides, which are attractive also as thermoelectric materials, and provides possible promising candidates for high-performance thermoelectric materials.

TABLE I. Space group of each oxide Ae_3TtO (Ae = Ca, Sr, Ba; Tt = Ge, Sn, Pb) in experiments. The abbreviations (HT) and (LT) denote the high-temperature and low-temperature phases, respectively. Information for Ba_3GeO and Sr_3GeO is taken from Refs. [61] and [62], respectively, and other information is taken from Ref. [63]. The transition temperatures of Ca_3GeO, Ba_3SnO, and Ba_3PbO are reported to be around 350, 150, and 150 K, respectively [63].

$Tt\backslash Ae$	Ca	Sr	Ba
Ge	$Pm\bar{3}m$ (HT), *Imma* (LT)	*Pnma*	*Pnma*
Sn	$Pm\bar{3}m$	$Pm\bar{3}m$	$Pm\bar{3}m$ (HT), *Imma* (LT)
Pb	$Pm\bar{3}m$	$Pm\bar{3}m$	$Pm\bar{3}m$ (HT), *Imma* (LT)

TABLE II. Space group of each nitride Ae_3PnN (Ae = Ca, Sr, Ba; Pn = As, Sb, Bi) in experiments. The abbreviations (HT) and (LT) denote the high-temperature and low-temperature phases, respectively. Information for Pn = Sr and Ba is taken from Ref. [64] and that for Pn = Ca is taken from Refs. [65] and [66]. The transition temperature of Ca_3AsN is reported to be 1025 K [65].

$Pn\backslash Ae$	Ca	Sr	Ba
As	$Pm\bar{3}m$ (HT), *Pnma* (LT)	...	...
Sb	$Pm\bar{3}m$	$Pm\bar{3}m$	$P6_3/mmc$
Bi	$Pm\bar{3}m$	$Pm\bar{3}m$	$P6_3/mmc$

This paper is organized as follows. Section II presents the calculation methods that we employ in this study. Our calculation results for the antiperovskite oxides and nitrides with the cubic ($Pm\bar{3}m$) structure are presented in Secs. III A and III B, respectively. In Sec. III C, the thermoelectric performance of the antiperovskite oxides and nitrides with the orthorhombic (*Imma* and *Pnma*) and hexagonal ($P6_3/mmc$) structures are discussed. This study is summarized in Sec. IV.

II. CALCULATION METHODS

First, we perform the structural optimization using the PBEsol exchange-correlation functional [67] and the projector augmented wave method [68] with the inclusion of the spin-orbit coupling (SOC). For this purpose, we use the Vienna Ab Initio Simulation Package (VASP) [69–72]. For the $Pm\bar{3}m$, *Imma*, *Pnma*, and $P6_3/mmc$ space groups, $12 \times 12 \times 12$, $10 \times 10 \times 10$, $10 \times 6 \times 10$, and $12 \times 12 \times 12$ **k**-meshes are used, respectively. Crystal structures of antiperovskites with these space groups are shown in Fig. 1. A plane-wave cutoff energy of 550 eV is used for all the cases.

After the structural optimization, we perform first-principles band-structure calculation using WIEN2K code [73]. We employ the Tran-Blaha modified Becke-Johnson (TBMBJ) potential [74,75] to obtain a reliable size of the band gap. In self-consistent-field (SCF) calculations for the $Pm\bar{3}m$, *Imma*, *Pnma*, and $P6_3/mmc$ space groups, $12 \times 12 \times 12$, $10 \times 10 \times 10$, $8 \times 6 \times 8$, and $10 \times 10 \times 10$ **k**-meshes arre used, respectively. For calculating DOS, we take $54 \times 54 \times 54$ and $38 \times 27 \times 38$ **k**-meshes for the $Pm\bar{3}m$ and *Pnma* space groups, respectively. We use a relatively high value of the $RK_{\max}$ parameter, 10, since Wannier functions in a high-energy region are extracted as mentioned below. SOC is included unless noted.

From the calculated band structures, we extract the Wannier functions of the Ae-d, $Tt(Pn)$-p, and O(N)-p orbitals using the WIEN2WANNIER and WANNIER90 codes [76–79]. We do not perform the maximal localization procedure for

the Wannier functions to prevent orbital mixing among the different spin components. For the $Pm\bar{3}m$, *Imma*, *Pnma*, and $P6_3/mmc$ space groups, we use $16 \times 16 \times 16$, $12 \times 12 \times 12$, $12 \times 8 \times 12$, and $10 \times 10 \times 10$ **k**-meshes, respectively, for constructing the Wannier functions. Then, we construct the tight-binding model with the obtained hopping parameters among the Wannier functions. We analyze the transport properties using this model with the Boltzmann transport theory. The transport coefficients K_ν are represented as follows:

$$\mathsf{K}_\nu = \tau \sum_{n,\mathbf{k}} \mathbf{v}_{n,\mathbf{k}} \otimes \mathbf{v}_{n,\mathbf{k}} \left[-\frac{\partial f_0}{\partial \epsilon_{n,\mathbf{k}}} \right] [\epsilon_{n,\mathbf{k}} - \mu(T)]^\nu, \quad (1)$$

with the Fermi-Dirac distribution function f_0; chemical potential $\mu(T)$; energy $\epsilon_{n,\mathbf{k}}$ and group velocity $\mathbf{v}_{n,\mathbf{k}}$ of the one-electron orbital on the nth band at the **k**-point **k**; and the relaxation time τ, which is assumed to be constant in this study. By using K_ν, the electrical conductivity σ, Seebeck coefficient S, and electrical thermal conductivity κ_{el} are expressed as follows:

$$\sigma = e^2 \mathsf{K}_0, \quad \mathsf{S} = -\frac{1}{eT} \mathsf{K}_0^{-1} \mathsf{K}_1, \quad (2)$$

$$\kappa_{\mathsf{el}} = \frac{1}{T} \left[\mathsf{K}_2 - \mathsf{K}_1 \mathsf{K}_0^{-1} \mathsf{K}_1 \right], \quad (3)$$

where e (> 0) is the elementary charge. The power factor (PF) equals σS^2 and the dimensionless figure of merit $ZT = \sigma S^2 T \kappa^{-1}$ are also calculated using these quantities. We assume that the thermal conductivity κ can be represented as the sum of the electrical thermal conductivity κ_{el} and the lattice electrical thermal conductivity κ_{lat}, namely, $\kappa = \kappa_{\mathrm{el}} + \kappa_{\mathrm{lat}}$. In our study, τ and κ_{lat} are assumed to be 10^{-14} s and $2\,\mathrm{Wm^{-1}\,K^{-1}}$, respectively, which are typical values for thermoelectric materials. In fact, the thermal conductivity of Ca_3SnO was reported to be around $2\,\mathrm{Wm^{-1}\,K^{-1}}$ at room temperature [47]. The relaxation time and the lattice thermal conductivity are generally different among materials, so their theoretical evaluation based on phonon calculation is an important future issue. In this study, we concentrate on how favorable the electronic band structure of the candidate materials is. We discuss this point in more detail through the comparison with the experimental results in Sec. III A 2.

To simulate the carrier doping, we adopt the rigid band approximation. Because an angle-resolved photoemission spectroscopy (ARPES) experiment on the Dirac semimetallic Ca_3PbO [80] reported that the band structure for hole-doped Ca_3PbO, say, $Ca_3Pb_{0.92}Bi_{0.08}O$, shows very good agreement with the calculated band structure for the mother compound Ca_3PbO, we can expect that the rigid-band approximation is valid against a certain level of the carrier doping, even for the narrow- or zero-gap systems. We only consider the hole carrier doping, which was realized in experiments for some antiperovskite oxides [36,47]. We employ a fine **k**-mesh up to $900 \times 900 \times 900$ for calculating the transport properties with sufficient convergence.

III. RESULTS AND DISCUSSIONS

A. Oxides Ae_3TtO with the cubic structure

In this section, we investigate the electronic structure and the transport properties of the antiperovskite oxides Ae_3TtO (Ae = Ca, Sr, Ba; Tt = Ge, Sn, Pb), assuming the cubic structure with a space group $Pm\bar{3}m$ for all the compounds. Because some oxides have a distorted crystal structure as shown in Table I, we see the effect of the structural (orthorhombic) distortion on thermoelectric performance in Sec. III C.

1. Band structures

Figure 2 presents a calculated band structure and partial DOS (PDOS) of Ba_3PbO with the cubic structure (space group $Pm\bar{3}m$) as a typical member of the antiperovskite oxides. Black broken and red solid lines in the band structure represent the band structures obtained with the first-principles calculation and the tight-binding model for the Wannier functions, respectively. As is clearly seen, the band structure calculated with the tight-binding model well reproduces the first-principles one near the Fermi energy, which validates our approach using the tight-binding model to evaluate the transport properties. It is characteristic that the valence and conduction bands near the Fermi energy mainly consist of the Tt(Pb)-p and Ae(Ba)-d orbitals, respectively [36]. In other words, a peculiar valence state Tt^{4-} is realized here. Another characteristic

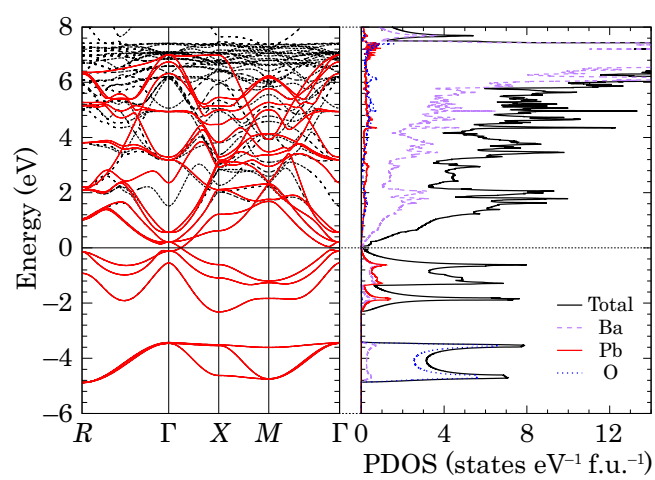

FIG. 2. Band structure and partial DOS (PDOS) of Ba_3PbO with the cubic structure (space group $Pm\bar{3}m$). Black broken and red solid lines in the band structure represent the band structures obtained with the first-principles calculation and the tight-binding model for the Wannier functions, respectively.

is the sixfold-degenerate Dirac cones along the Γ-X line near the Fermi energy. This degeneracy originates from the crystal symmetry.

Figure 3 presents the band structures of various antiperovskite oxides, which show that the existence of the band gap and the Dirac cones depends on the constituent elements. The atomic replacement of $Tt = \mathrm{Ge} \rightarrow \mathrm{Sn} \rightarrow \mathrm{Pb}$ naturally leads to reduction of the band gap for $Ae = \mathrm{Ca}$ and Sr, owing to an upward shift of the valence-band dispersion, mainly consisting of the Tt-atomic orbitals. This atomic replacement also enhances SOC, the effect of which is investigated later in this paper. Here, we only point out that the valence-band splitting at the Γ point induced by SOC becomes larger by this atomic replacement as shown in Fig. 3.

Quasi-one-dimensionality of the valence-top band structure of some materials is noteworthy. For example, the valence-top band structure of Ca_3GeO shown in Fig. 3(a) consists of a nearly degenerate band dispersion with a heavy effective mass and another one with a much lighter mass along the Γ-X line. Concretely, the ratio of the effective masses along the Γ-X line for the top three (six when considering the spin degeneracy) valence bands is 3.1:0.49:1 for Ca_3GeO. This feature corresponds with the fact that there are three quasi-one-dimensional band dispersions that are mobile along one of the x, y, and z directions, respectively. Such a quasi-one-dimensionality originates from the anisotropy of the Tt-p orbitals. Because low dimensionality is desirable for high thermoelectric performance [26–29] owing to its large DOS near the band edge together with a sizable group velocity to a specific direction, the quasi-one-dimensionality in antiperovskites can be an advantageous feature for thermoelectric performance.

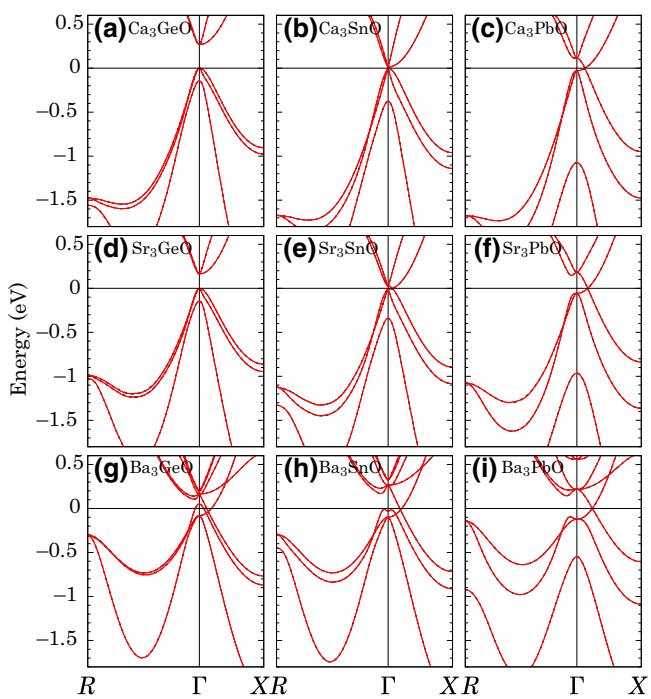

FIG. 3. Band structures of Ae_3TtO ($Ae = \mathrm{Ca, Sr, Ba}$; $Tt = \mathrm{Ge, Sn, Pb}$) with the cubic structure (space group $Pm\bar{3}m$): (a) Ca_3GeO, (b) Ca_3SnO, (c) Ca_3PbO, (d) Sr_3GeO, (e) Sr_3SnO, (f) Sr_3PbO, (g) Ba_3GeO, (h) Ba_3SnO, and (i) Ba_3PbO. Black broken and red solid lines represent the band structures obtained with the first-principles calculation and the tight-binding model for the Wannier functions, respectively.

We note that, while each band dispersion has anisotropy along one of the x, y, and z directions, the coexistence of these three bands results in the isotropy of the transport property, which is naturally expected for the cubic structure. Even though the transport is in total isotropic, the situation is much different from the case when two isotropic heavy bands coexist with one isotropic light band. Because, for the latter case, the carrier with a large DOS has a heavy effective mass along all the directions, it is not accompanied with a large group velocity. For a more detailed investigation of this kind of band structure, i.e., coexisting low-dimensional bands with anisotropy along different directions, we refer the reader to Ref. [81]. We also note that, in real one-dimensional systems, technological applications are not straightforward because they require high orientation of samples, without which the conductivity is easily lost. Low dimensionality owing to the anisotropy of the electron wave function realized in a rather isotropic crystal structure, like our target materials here, is favorable from this perspective [81–84] because the conductivity is expected to be kept without a very high orientation of samples.

2. Thermoelectric performance: Comparison with experiment

Before proceeding to the investigation on thermoelectric performance among antiperoviskite oxides, we check the consistency between our calculated values of the transport quantities and those reported in an experimental study. In Ref. [47], $\rho = 7.3\,\mathrm{m\Omega\,cm}$ and $S = 94\ \mu\mathrm{V\,K^{-1}}$ were reported for polycrystalline Ca_3SnO at 290 K. The carrier density was also estimated from the Hall coefficients, $n = 1.44 \times 10^{19}$ and $1.43 \times 10^{19}\ \mathrm{cm^{-3}}$ at 5 and 20 K, respectively. In our calculation for Ca_3SnO, we obtain $\rho\tau = 3.5 \times 10^{-14}\,\mathrm{m\Omega\,cm\,s}$ and $S = 88\ \mu\mathrm{V\,K^{-1}}$ using the carrier density $n = 1.43 \times 10^{19}\ \mathrm{cm^{-3}}$ at 290 K. The agreement with the experimental Seebeck coefficient ($94\ \mu\mathrm{V\,K^{-1}}$) is surprisingly good. In addition, we can roughly estimate the relaxation time τ as 4.8×10^{-15} s, by taking a ratio of the calculated $\rho\tau$ and the experimental ρ. This is a typical length of the relaxation time for thermoelectric materials.

In the experimental study of Ref. [47], $\rho = 2.5\,\mathrm{m\Omega\,cm}$ and $S = 22\ \mu\mathrm{V\,K^{-1}}$ at 290 K for polycrystalline Ca_3PbO were also reported. For Ca_3PbO, we determine the carrier density so as to provide the Seebeck coefficient $S =$

22 μV K^{-1} at 290 K, which is the same value with the experimental Seebeck coefficient. We obtain the carrier density $n = 3.3 \times 10^{20}$ cm^{-3} and the calculated electrical resistivity for that carrier density is $\rho\tau = 3.4 \times 10^{-15}$ mΩ cm s. Therefore, by comparing it with the experimental ρ, the relaxation time τ is estimated as 1.3×10^{-15} s. This length of the relaxation time is again typical for thermoelectric materials. While it is shorter than the value assumed in this study, a longer relaxation time can be expected in future experiments because the sample investigated in Ref. [47] was polycrystal.

By using the carrier density ($n = 1.43 \times 10^{19}$ cm^{-3} for Ca_3SnO and $n = 3.3 \times 10^{20}$ cm^{-3} for Ca_3PbO) and the relaxation time at 300 K ($\tau = 4.8 \times 10^{-15}$ s for Ca_3SnO and $\tau = 1.3 \times 10^{-15}$ s for Ca_3PbO) estimated above, we can compare the temperature dependence of the electrical resistivity and the Seebeck coefficient between experiment and calculation. Figure 4 presents the calculated electrical resistivity and the Seebeck coefficient and the experimental data taken from Ref. [47]. The calculated temperature dependence of the Seebeck coefficient shown in Fig. 4(b) is to some extent consistent with the experimental one for these two materials. Possible origins for the error shown here are the error in determining the carrier density, the difference in the crystal structure, and the accuracy of the calculated band structure.

A difference in the electrical resistivity between experiment and calculation shown in Fig. 4(a) likely originates from the temperature dependence of the relaxation time, which is ignored in calculation. For Ca_3SnO, the ratio of the electrical resistivity at 120 and 290 K, $\rho_{290\,\mathrm{K}}\rho_{120\,\mathrm{K}}^{-1}$, is 1.0 in calculation using the constant relaxation-time approximation and the carrier density $n = 1.4 \times 10^{19}$ cm^{-3}, while $\rho_{290\,\mathrm{K}}\rho_{120\,\mathrm{K}}^{-1} = 1.8$ in experiment [47]. This difference suggests that $\tau_{120\,\mathrm{K}}\tau_{290\,\mathrm{K}}^{-1}$ is about 1.8 (= 1.8/1.0). On the other hand, the thermal conductivity of Ca_3SnO reported in Ref. [47], which can be regarded as κ_{lat} because the electronic contribution of the thermal conductivity was reported to be negligible, is around 2.9 and 1.7 Wm^{-1} K^{-1} at 120 and 290 K, respectively. Thus, $\kappa_{\mathrm{lat},120\,\mathrm{K}}\kappa_{\mathrm{lat},290\,\mathrm{K}}^{-1}$ is about 1.7. Here, the calculated ZT within the constant relaxation-time approximation depends only on the ratio $\kappa_{\mathrm{lat}}\tau^{-1}$ because

$$ZT = \frac{\sigma S^2 T}{\kappa_{\mathrm{el}} + \kappa_{\mathrm{lat}}} = \frac{\sigma S^2 T \tau^{-1}}{\kappa_{\mathrm{el}}\tau^{-1} + \kappa_{\mathrm{lat}}\tau^{-1}}, \tag{4}$$

where both $\sigma S^2 T\tau^{-1}$ and $\kappa_{\mathrm{el}}\tau^{-1}$ depend on neither τ nor on κ_{lat}. Since $\kappa_{\mathrm{lat}}\tau^{-1}$ is expected to be roughly the same between $T = 120$ and 290 K as shown here, we can expect that the calculated temperature dependence of ZT is to some extent reliable. We note that the temperature dependence of τ and κ_{lat} in the high-temperature region is at present not available in experiment. Therefore, the calculated temperature dependence of ZT beyond room temperature still has some uncertainty regarding these assumed values of τ and κ_{lat}.

3. Thermoelectric performance: Calculation

Figure 5 presents the calculated ZT values of the antiperovskite oxides with the cubic ($Pm\bar{3}m$) structure. Broken lines in the figure correspond to materials that have yet to be synthesized in the structure with the $Pm\bar{3}m$ space group. The hole-carrier concentration is optimized for each point, so it depends on temperature in this plot.

In the high-temperature region, Ca_3GeO yields the highest ZT, where the quasi-one-dimensional band structure together with a finite band gap is realized as shown in Fig. 3(a). This result seems to be natural because of the superiority of the low-dimensional electronic structure for thermoelectric performance as described in the previous

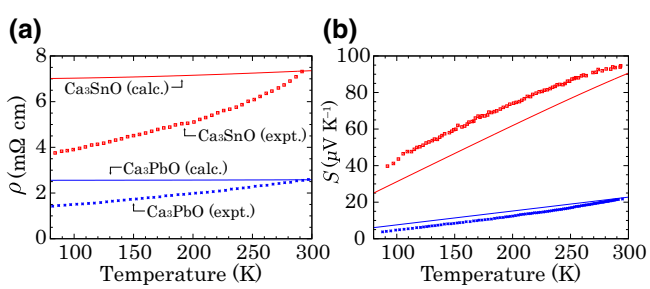

FIG. 4. (a) Electrical resistivity obtained by our calculation and experimental data taken from Ref. [47] for Ca_3SnO and Ca_3PbO. (b) Those for the Seebeck coefficient. In calculation, we use the carrier density $n = 1.43 \times 10^{19}$ cm^{-3} for Ca_3SnO and $n = 3.3 \times 10^{20}$ cm^{-3} for Ca_3PbO, and the constant relaxation time $\tau = 4.8 \times 10^{-15}$ s for Ca_3SnO and $\tau = 1.3 \times 10^{-15}$ s for Ca_3PbO, which are determined from the comparison with experiment and calculation as described in the main text.

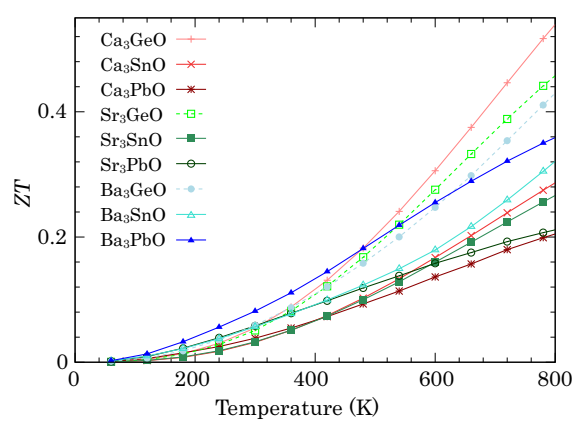

FIG. 5. Calculated ZT values of Ae_3TtO (Ae = Ca, Sr, Ba; Tt = Ge, Sn, Pb) with the cubic structure (space group $Pm\bar{3}m$) with respect to temperature. Broken lines correspond to materials that have yet to be synthesized in the structure with the $Pm\bar{3}m$ space group. The hole-carrier concentration is optimized for each point.

section. In addition, the band gap prevents cancellation of the contribution from the electron and hole carriers in the transport coefficient K_1, Eq. (1), appearing in the Seebeck coefficient, Eq. (2).

On the other hand, in the low-temperature region, it is rather counterintuitive that Ba_3PbO yields the highest ZT. In its band structure shown in Fig. 3(i), there are Dirac cones at the Fermi energy without the gap. As mentioned in the previous paragraph, the band dispersion without the gap is generally not favorable for thermoelectric performance because of the cancellation of the electron and hole carrier transport. In the next section, we investigate how the Dirac cones in Ba_3PbO result in the high thermoelectric performance.

4. How do the Dirac cones in Ba_3PbO enhance the thermoelectric performance?

To begin with, we investigate the effect of SOC on the thermoelectric performance. Figure 6 presents the calculated band structure of Ba_3PbO without the inclusion of SOC. Although the Dirac cones are preserved along the Γ-X line, the system becomes metallic (i.e., a finite-size Fermi surface takes place) without SOC as seen in the band dispersion along the Γ-R line. A metallic electronic structure is clearly unfavorable for thermoelectric performance. In fact, the maximum value of ZT with respect to the hole carrier concentration is 0.04 for $T = 300$ K when SOC is switched off, which is only half of $ZT = 0.08$ when SOC is included in the calculation. Therefore, SOC is one of the indispensable factors for high thermoelectric performance of Ba_3PbO.

To obtain more insight, we compare several transport quantities for three cases: Ba_3PbO, Sr_3PbO, and Ca_3GeO. From here on, we again include SOC in the calculations. Among these three compounds, Ba_3PbO and Sr_3PbO have Dirac cones, while Ca_3GeO is an insulator with a gap as shown in Figs. 3(a), 3(f), and 3(i). The Dirac cones without the gap allow the cancellation of the electron and hole carrier contribution for the Seebeck coefficient S when the carrier concentration is low, which is verified by our calculation results at 300 K as shown in Fig. 7. However, we also notice that the Seebeck coefficient becomes comparable for these three materials when the chemical potential is sufficiently far from $\mu = 0$ and when ZT and PF reach their maximum values in such a region. In fact, even for Ba_3PbO and Sr_3PbO, the Seebeck coefficient can exceed 100 μV K^{-1}. This is one of the reasons why the relatively large values of ZT and PF can be achieved for the nongap band dispersion for these materials. We note that, at high temperatures, the cancellation of the electron and hole carrier contribution occurs for a wider carrier concentration, and so ZT of Ba_3PbO with the nongapped Dirac cones is, in fact, much lower than that of Ca_3GeO with the gapped band structure as we see in Fig. 5.

By looking into the electrical conductivity σ and the Seebeck coefficient S shown in Fig. 7, a superiority of Ba_3PbO among the three materials can be seen for its high electrical conductivity. A key characteristic of its band structure around $\mu = -0.08$ eV, where ZT and PF are maximized, is the high valley degeneracy. First, the Dirac

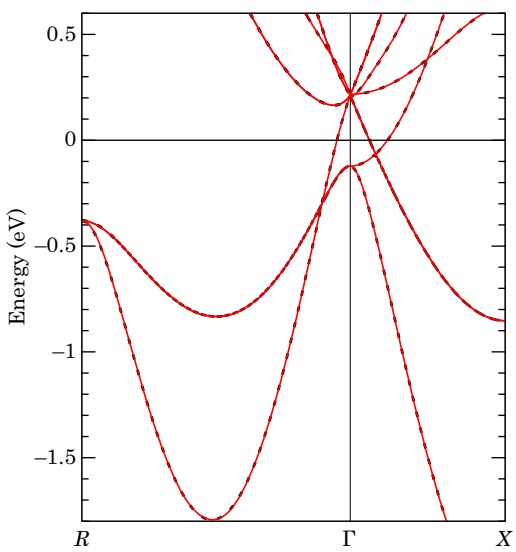

FIG. 6. Band structures of Ba_3PbO with the cubic structure (space group $Pm\bar{3}m$). The calculation is performed without the inclusion of SOC. Black broken and red solid lines represent the band structures obtained with the first-principles calculation and the tight-binding model for the Wannier functions, respectively.

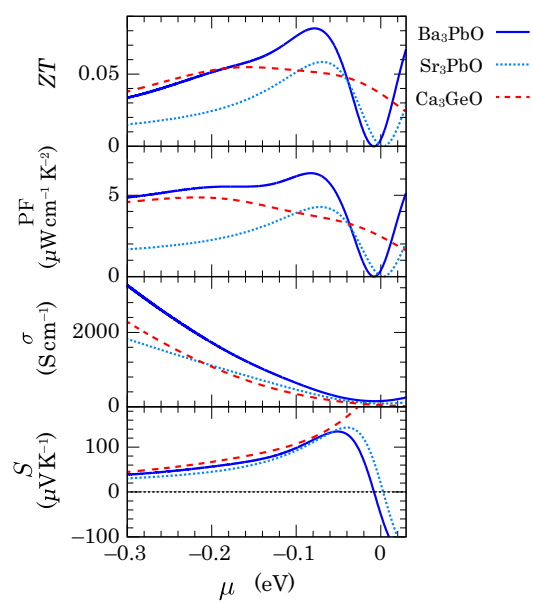

FIG. 7. Calculated ZT, PF, σ, and S at 300 K for Ba_3PbO, Sr_3PbO, and Ca_3GeO with the cubic structure (space group $Pm\bar{3}m$). The Fermi energy without doped carriers is set to zero.

cones have sixfold degeneracy by the crystal symmetry. In addition, the valence-top band structure around the Γ and *R* points can enhance the thermoelectric performance by temperature broadening [see Fig. 3(i)]. On the other hand, the band structure without the Dirac cones as in Ca_3GeO has no valley degeneracy since there are no other **k**-points that are equivalent to the Γ point where the valence-band top resides. We note that, in Sr_3PbO, the *R* valley is too deep to enhance the thermoelectric performance while the Γ point can play a role, which is an important difference between Sr_3PbO and Ba_3PbO. It has been established that the multivalley band structure is favorable for high thermoelectric performance [25]. Therefore, the high valley degeneracy is an important advantage of Ba_3PbO. It is also interesting that the valence-band top at the Γ point for Ba_3PbO has a pudding-mold shape [33], which can enhance DOS near the band edge. This is another outcome of the large band deformation near the Fermi energy induced by SOC.

Before proceeding to the next section, we point out two issues regarding thermoelectric performance of the Dirac cone. First, one should pay attention to the applicability of the Boltzmann transport theory with the constant-relaxation-time approximation because it cannot appropriately deal with the interband scattering effects, which can affect thermoelectric properties of the systems where the bipolar effects are important such as those possessing the Dirac cone [85]. In our case, the chemical potential becomes sufficiently deep (approximately −0.1 eV) from the Dirac points at room temperature. Therefore, we expect that the interband scattering is not so dominant for our calculated results compared with the case when the chemical potential lies near the Dirac point, at least if the scattering strength is not so strong that the interband scattering becomes very active. Second, we point out that a possible long relaxation time is another advantage of the Dirac cones. This feature is naturally expected because a small DOS such as for the Dirac cone generally reduces the number of possible electron scattering processes and then yields a long relaxation time. However, these points regarding the scattering processes need further investigation and so are important future issues.

B. Nitrides Ae_3PnN with the cubic structure

Next, we move on to the antiperovskite nitrides with a chemical formula Ae_3PnN (Ae = Ca, Sr, Ba; Pn = As, Sb, Bi). In the same manner as the previous section, we assume the cubic structure with a space group $Pm\bar{3}m$ for all the compounds in this section. We see the thermoelectric performance of these materials with other crystal symmetries in Sec. III C.

1. Band structures

Figure 8 presents the whole band structure and PDOS of Sr_3SbN as a typical member of antiperovskite nitrides

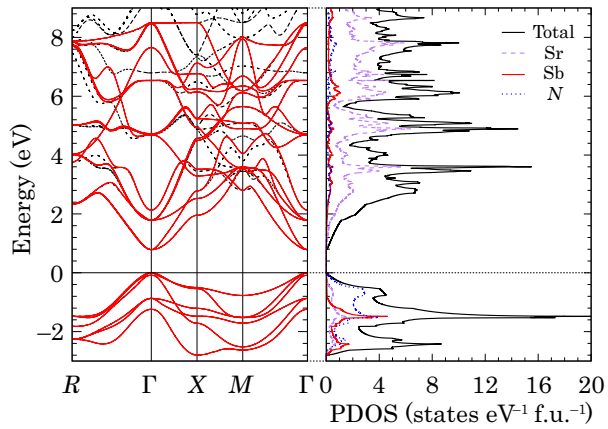

FIG. 8. Band structure and PDOS of Sr_3SbN with the cubic structure (space group $Pm\bar{3}m$). Black broken and red solid lines in the band structure represent the band structures obtained with the first-principles calculation and the tight-binding model for the Wannier functions, respectively.

Ae_3PnN. The most striking difference from oxides is that the valence-top band structure mainly consists of nitrogens, which holds also for other nitrides investigated in this study. This is because nitrogen atomic orbitals have shallower energy levels than oxygen atomic orbitals. In addition, *Pn* atomic orbitals have deeper energy levels than *Tt* atomic orbitals in the same period.

As a result, the band structures of the antiperovskite nitrides shown in Fig. 9 have different features from oxides. First of all, unlike the oxides, all the nitrides have a band gap. Therefore, there is no chance that the Dirac cones appear at the Fermi energy. On the other hand, we can recognize the low dimensionality of the valence-top band structure similar to that seen in Fig. 3(a). This observation corresponds to the fact that the three *p* orbitals of the nitrogens have anisotropy(quasi-one-dimensionality) for its conduction. We cover this point in more detail in the next section.

2. Thermoelectric performance

Calculated *ZT* values of the antiperovskite nitrides are shown in Fig. 10. Because of the low dimensionality and a sufficiently large band gap, calculated *ZT* values for nitrides are relatively high. However, we note that materials with high *ZT* values are not stable as the cubic structure. If one restricts the target materials to those existing as the cubic structure in experiment, which are shown with solid lines in Fig. 10, the maximum *ZT* value at 300 K is 0.08 for Sr_3SbN, which is comparable to that of Ba_3PbO, 0.08. Even under this restriction, at high temperatures, the estimated*ZT* values of some nitrides such as Sr_3SbN and Ca_3AsN exceed those of all the oxides calculated in this study.

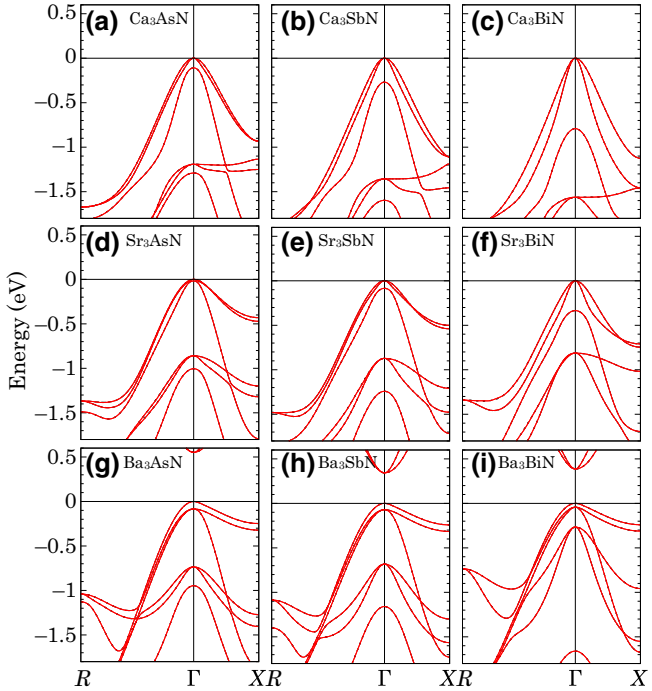

FIG. 9. Band structures of Ae_3PnN ($Ae = \mathrm{Ca, Sr, Ba}$; $Pn = \mathrm{As, Sb, Bi}$) with the cubic structure (space group $Pm\bar{3}m$): (a) Ca_3AsN, (b) Ca_3SbN, (c) Ca_3BiN, (d) Sr_3AsN, (e) Sr_3SbN, (f) Sr_3BiN, (g) Ba_3AsN, (h) Ba_3SbN, and (i) Ba_3BiN. Black Black broken and red solid lines represent the band structures obtained with the first-principles calculation and the tight-binding model for the Wannier functions, respectively.

Why do the crystal structures that are unstable as the cubic structure exhibit high ZT values in calculation? A key is the correlation between the strong quasi-one-dimensionality of the band structures of Sr_3AsN and Ba_3PnN ($Pn = \mathrm{As, Sb, Bi}$) and their high ZT values shown in Fig. 10. In other words, as shown in Figs. 9(d) and 9(g)–9(i), the ratio of the effective masses of the heavy and light band dispersions along the Γ-X line looks large for these compounds with high ZT values.

To see why these materials exhibit the strong quasi-one-dimensionality, we calculate the band structures of Ca_3AsN and Ba_3AsN using our tight-binding model from which the As orbitals are excluded. In other words, the tight-binding Hamiltonian consisting only of the Ae and N orbitals is solved here. The obtained band structures are shown with red solid lines in Fig. 11 and compared with the original band structures shown with black dotted lines. While the valence-top band structure of Ba_3AsN shown in Fig. 11(b) is almost unaffected by neglecting the As orbitals, we find that the low dimensionality of the nitrogen bands in Ca_3AsN is much degraded by hybridization with the As orbitals as shown in Fig. 11(a). Concretely, the ratios of the effective masses along the Γ-X line for the top three (six when considering the spin degeneracy) valence bands in Fig. 11 are 1.5:0.64:1 for the original Ca_3AsN, 1.3:1.3:1 for the Ca_3AsN without the Wannier orbitals of As, 1.7:3.4:1 for the original Ba_3AsN, and 1.6:3.6:1 for the Ba_3AsN without the Wannier orbitals of As. This difference can be naturally understood because, in Ba_3AsN, the Ba ionic radius may be too large to keep the As-N distance short enough to hybridize, which preserves the low dimensionality of the nitrogen orbitals. Therefore, this strong low dimensionality is in accord with the instability of the crystal structure. In general, the structural instability might enhance the anharmonicity of phonons, which often reduces the lattice thermal conductivity and then enhances ZT. It is interesting that the structural instability and the improvement of the electronic band structure,

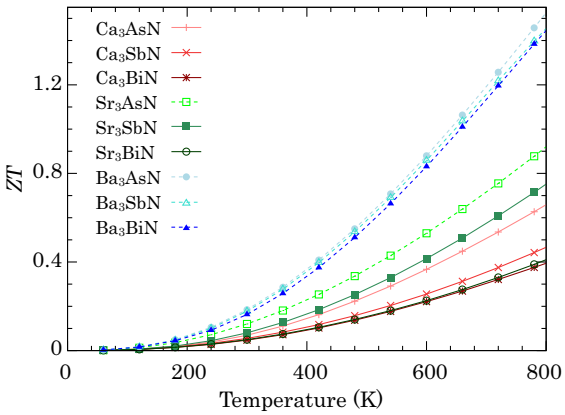

FIG. 10. Calculated ZT values of Ae_3PnN ($Ae = \mathrm{Ca, Sr, Ba}$; $Pn = \mathrm{As, Sb, Bi}$) with the cubic structure (space group $Pm\bar{3}m$) with respect to temperature. Broken lines correspond to materials that have yet to be synthesized in the structure with the $Pm\bar{3}m$ space group. The hole carrier concentration is optimized for each point.

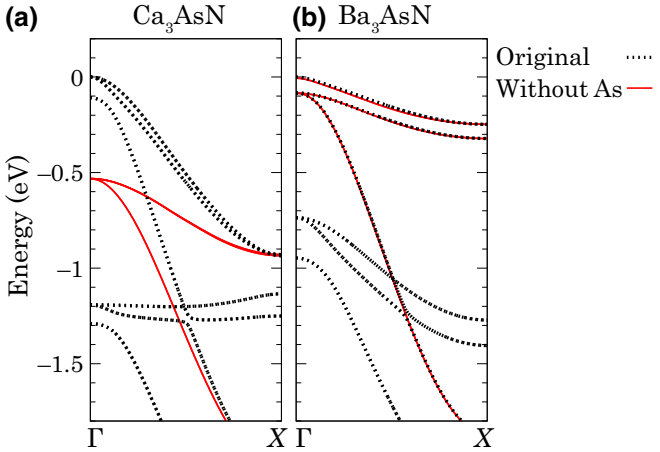

FIG. 11. Band structures calculated using the tight-binding model for (a) Ca_3AsN and (b) Ba_3AsN. Black dotted and red solid lines represent the original band structure and that calculated without the As orbitals, respectively.

both of which might be favorable for ZT, can occur simultaneously in the antiperovskite nitrides. We note that this expectation should be checked carefully because there are other factors involved with ZT such as a change in the electron relaxation time by increasing the structural instability. First-principles evaluation of these quantities is an interesting future issue.

C. Thermoelectric performance with the orthorhombic and hexagonal structures

In this section, we investigate thermoelectric performance of the antiperovskite oxides and nitrides with the orthorhombic and hexagonal structures. For this purpose, we first evaluate which structure among the experimentally observed space groups is the most stable for each nitride because some nitrides have yet to be synthesized in experiment, unlike the oxides. After that, we discuss the effect of the structural change from the cubic structure on thermoelectric performance. The temperature dependence of ZT for the most promising candidates that we find is also presented.

1. Stability of the Pm$\bar{3}$m phase

We investigate the structural stability of the $Pm\bar{3}m$ phase for the nitrides by comparing its total energy with that of the *Pnma* and $P6_3/mmc$ phases. Figure 12 presents the total energies of the *Pnma* and $P6_3/mmc$ phases, relative to that of the $Pm\bar{3}m$ phase, for the antiperovskite nitrides. Because *Pnma* is a subgroup of $Pm\bar{3}m$, the zero relative energy of the former to the latter means that the crystal structure becomes $Pm\bar{3}m$ in calculation even when one allows the crystal distortion that can take place for the *Pnma* space group. To be more precise, when the total energy difference of these two phases is less than 0.1 meV f.u.$^{-1}$, we regard the crystal structure of the *Pnma* phase that falls into the $Pm\bar{3}m$ phase. Materials with the $Pm\bar{3}m$ phase as the most stable structure are shaded by color in the figure. We note that, because *Pnma* is a subgroup of *Imma*, we need not calculate the total energy of the *Imma* phase to discuss the stability of the cubic structure. In addition, we verify that the optimized crystal structures for AeAsN$_3$ and BaSbN$_3$ no longer have the full *Imma* symmetry; i.e., the crystal structure seems to fall into the *Pnma* phase for these compounds.

Our results presented in Fig. 12 show surprisingly good agreement with the experimental observation listed in Table II, with respect to the most stable structure of each compound. In addition, the experimental observation that Ca$_3$AsN becomes $Pm\bar{3}m$ at high temperature is also consistent with a small energy difference between the *Pnma* and $Pm\bar{3}m$ phases in our calculation. It is characteristic that the $Pm\bar{3}m$ phase in all the $Ae = $ Ba compounds is much more unstable than the $P6_3/mmc$ phase. We find that the unsynthesized Sr$_3$AsN and Ba$_3$AsN are likely to be the *Pnma* and $P6_3/mmc$ phases, respectively. Because Sr$_3$AsN with the *Pnma* structure is a good candidate for high-performance thermoelectric material as we see later in this paper, we also perform the phonon calculation to verify the stability of this structure. For this purpose, we employ the finite displacement method as implemented in the PHONOPY [86] software in combination with VASP. We use a $2 \times 2 \times 2$ **q**-mesh without including the spin-orbit coupling because Sr$_3$AsN consists of relatively light elements. We use a $4 \times 3 \times 4$ **k**-mesh for calculation of the corresponding $(2 \times 2 \times 2)$ supercell. Figure 13 presents the calculated phonon dispersion of Sr$_3$AsN with the *Pnma*

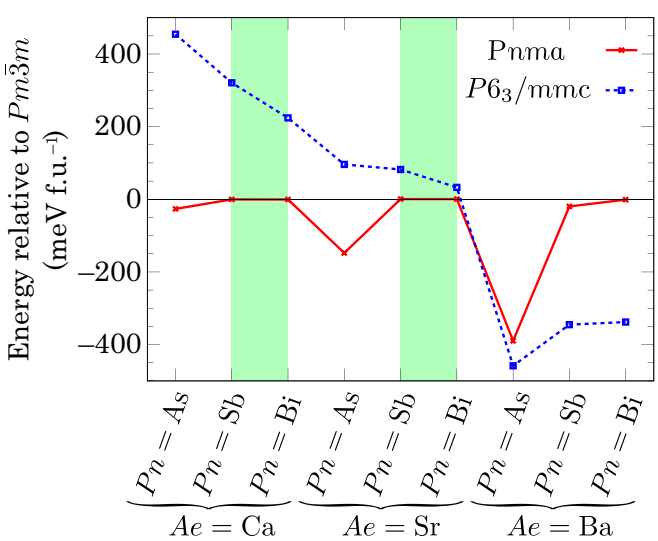

FIG. 12. Total energies of the *Pnma* and $P6_3/mmc$ phases relative to that of the $Pm\bar{3}m$ for Ae_3PnN ($Ae = $ Ca, Sr, Ba; $Pn = $ As, Sb, Bi). Materials where $Pm\bar{3}m$ is the most stable in our calculation (see the main text for more detail) are shaded by color.

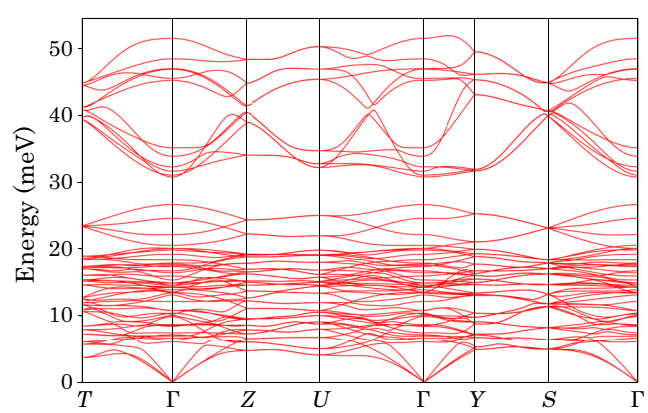

FIG. 13. Phonon dispersion of Sr$_3$AsN in the *Pnma* phase. The **k**-points represented with the crystal coordinates are as follows: $T = (\mathbf{b}^* + \mathbf{c}^*)/2$, $Z = \mathbf{c}^*/2$, $U = (\mathbf{a}^* + \mathbf{c}^*)/2$, $Y = \mathbf{b}^*/2$, and $S = (\mathbf{a}^* + \mathbf{b}^*)/2$.

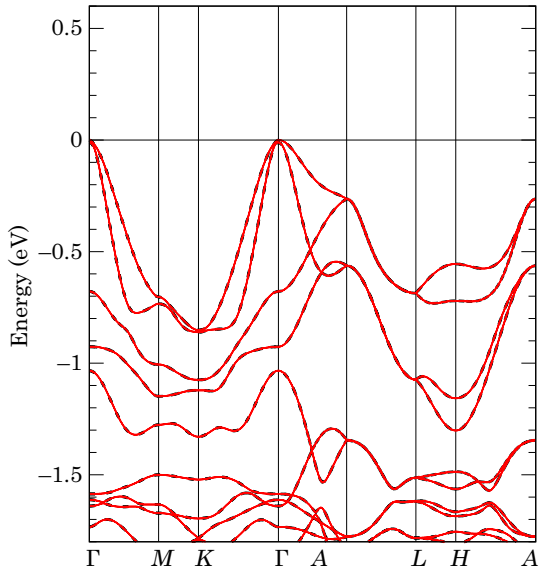

FIG. 14. Band structures of Ba_3BiN with the hexagonal structure (space group $P6_3/mmc$). Black broken and red solid lines represent the band structures obtained with the first-principles calculation and the tight-binding model for the Wannier functions, respectively.

structure. Because no imaginary modes appear here, we can conclude that this structure is dynamically stable [87].

We next investigate the thermoelectric performance of materials with hexagonal and orthorhombic structures. On the basis of the above calculation results shown in Fig. 12 for nitrides and the experimental observation shown in Table I for oxides, we focus on materials that are stable in these structures rather than in the cubic phase.

2. Hexagonal structure

Figure 14 presents the band structure of Ba_3BiN with the hexagonal structure(space group $P6_3/mmc$). Compared with that for the cubic structure as shown in Fig. 9(i), this band structure does not seem to be favorable for thermoelectric performance because of the weakened anisotropy of the band dispersion near the valence-band top. As a matter of fact, the maximum value of ZT at 300 K is around 0.07 for the a and b directions and 0.05 for the c direction, which are less than a half of the ZT value for the cubic structure, 0.16. As shown in Table III, the situation is similar to Ba_3AsN and Ba_3SbN, for which the hexagonal structure is the most stable in our calculation presented in the previous section.

Whereas the electronic band structure is unfavorable for thermoelectric performance, a possible rattling motion [13, 15–22] of the Pn atoms, which can reduce the lattice thermal conductivity and thus increase ZT, is intriguing in the hexagonal phase [88].

TABLE III. Calculated ZT values of cubic and hexagonal Ba_3PnN at 300 K. Hole carrier concentration is optimized for each condition.

	Cubic	Hexagonal	
Lattice axis	$a = b = c$	$a = b$	c
Ba_3AsN	0.18	0.11	0.11
Ba_3SbN	0.18	0.06	0.10
Ba_3BiN	0.16	0.07	0.05

TABLE IV. Calculated ZT values of the cubic ($Pm\bar{3}m$) and orthorhombic (*Imma*) structures at 300 K. Calculation results are only shown for materials for which the *Imma* structure is experimentally reported. Hole carrier concentration is optimized for each condition.

	Cubic	Orthorhombic (*Imma*)		
Lattice axis	$a = b = c$	a	b	c
Ca_3GeO	0.05	0.07	0.06	0.06
Ba_3SnO	0.06	0.05	0.05	0.05
Ba_3PbO	0.08	0.06	0.06	0.07

3. Orthorhombic structures

Tables IV and V present the calculated ZT values for the orthorhombic (*Imma* and *Pnma*, respectively) structures at 300 K, compared with those for the cubic ($Pm\bar{3}m$) structure. Overall, the calculated ZT values are similar between the cubic and orthorhombic phases for each compound. However, we can see a notable increase in ZT by introducing the orthorhombic distortion for two materials: ZT increases from 0.06 in $Pm\bar{3}m$ to 0.18 (a axis), 0.20 (b axis), and 0.26 (c axis) in *Pnma* for Ba_3GeO, and from 0.12 in $Pm\bar{3}m$ to 0.18 (a axis), 0.20 (b axis), and 0.16 (c axis) in *Pnma* for Sr_3AsN. We then focus on these two materials in the following analysis. While Ba_3AsN also exhibits large

TABLE V. Calculated ZT values of the cubic ($Pm\bar{3}m$) and orthorhombic (*Pnma*) structures at 300 K. Calculation results are only shown for materials for which the *Pnma* structure is experimentally reported or predicted to be stable by our calculation as presented in Fig. 12. While the hexagonal structure is the most stable in our calculation for Ba_3AsN, ZT values in the *Pnma* phase are also shown for this compound because the total energies of the orthorhombic and hexagonal structures are comparable in Fig. 12. Hole carrier concentration is optimized for each condition.

	Cubic	Orthorhombic (*Pnma*)		
Lattice axis	$a = b = c$	a	b	c
Sr_3GeO	0.05	0.07	0.07	0.08
Ba_3GeO	0.06	0.18	0.20	0.26
Ca_3AsN	0.07	0.07	0.07	0.06
Sr_3AsN	0.12	0.18	0.20	0.16
Ba_3AsN	0.18	0.15	0.20	0.16

ZT values in the *Pnma* phase, these values are similar to that in the cubic phase, and in addition, the total energy of the *Pnma* phase is higher than that in the hexagonal phase as shown in Fig. 12. If synthesized in the *Pnma* phase, Ba_3AsN can also be a promising thermoelectric material.

In Ba_3GeO with the *Pnma* phase, the structure of which is shown in Fig. 1(c), optimized lattice constants are $a = 7.609$, $b = 10.697$, and $c = 7.481$ Å. The strength of the lattice distortion from the cubic lattice can be evaluated from the ratios $b(\sqrt{2}c)^{-1} = 101.1\%$ and $ac^{-1} = 101.7\%$, both of which are 100% for the structure without the orthorhombic distortion because the *Pnma* phase has a $\sqrt{2} \times \sqrt{2} \times 2$-times enlarged unit cell compared with that for the $Pm\bar{3}m$ phase. These structural parameters are roughly consistent with the experimental values measured at 296 K [61], $a = 7.591(1)$, $b = 10.728(1)$, $c = 7.551(1)$ Å, $b(\sqrt{2}c)^{-1} = 100.5\%$, and $ac^{-1} = 100.5\%$. The average bonding angle of O-Ba-O is 155.0° in our calculation and 158.4° in the experiment, which also show good agreement.

Figure 15(a) presents the band structure of Ba_3GeO in the *Pnma* phase. The most important change from that in the $Pm\bar{3}m$ phase shown in Fig. 3(g) is the gap opening, which is an important reason for the strong enhancement in *ZT*. In addition, we can see an approximate but high valley degeneracy near the valence-band top in Fig. 15(a), which should be another cause of the high performance through the resulting large DOS. A possibly related feature for the high valley degeneracy can be found in the $Pm\bar{3}m$ phase: the energy level of the valley at the *R* point is relatively close to that at the Γ point as shown in Fig. 3(g). We note that the *R* point in the $Pm\bar{3}m$ phase is folded into the Γ point in the*Pnma* phase. We can also notice that the quasi-one-dimensionality of the valence-band structure in the $Pm\bar{3}m$ phase, which seems comparable to that for Ca_3GeO, likely plays an important role for the high *ZT* of Ba_3GeO in the *Pnma* phase.

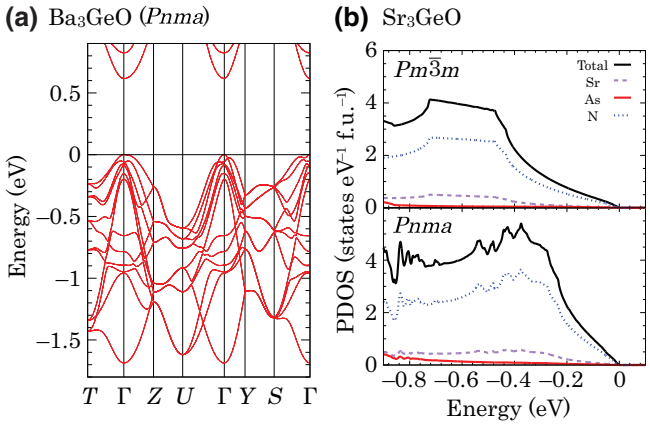

FIG. 15. (a) Band structure of Ba_3GeO in the *Pnma* phase. Black broken and red solid lines in the band structure represent the band structures obtained with the first-principles calculation and the tight-binding model for the Wannier functions, respectively. The **k**-points represented with the crystal coordinate are as follows: $T = (\mathbf{b}^* + \mathbf{c}^*)/2$, $Z = \mathbf{c}^*/2$, $U = (\mathbf{a}^* + \mathbf{c}^*)/2$, $Y = \mathbf{b}^*/2$, and $S = (\mathbf{a}^* + \mathbf{b}^*)/2$. (b) DOS near the valence-band top for Sr_3GeO in the $Pm\bar{3}m$ (top) and *Pnma* (bottom) phases.

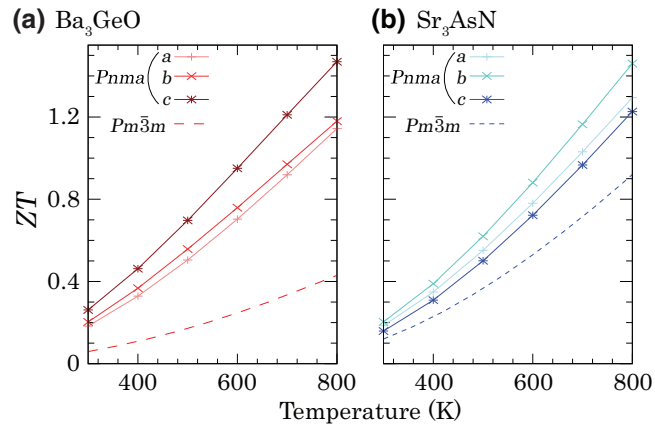

FIG. 16. Temperature dependence of *ZT* for (a) Ba_3GeO and (b) Sr_3AsN. For the *Pnma* phase, *ZT* values for each axis are shown. The hole carrier concentration is optimized for each point.

Figure 15(b) presents the calculated DOS of Sr_3AsN in the $Pm\bar{3}m$ and *Pnma* phases. While both phases have a gapped band structure, DOS near the valence-band top is again enhanced by the structural distortion, which is likely to be an origin of the high *ZT*. Because the overall shape of DOS is similar between these two phases, the increase in *ZT* for Sr_3AsN is moderate compared with Ba_3GeO.

We also calculate the temperature dependence of *ZT* for Ba_3GeO and Sr_3AsN in the $Pm\bar{3}m$ and *Pnma* phases, as shown in Fig. 16. The resulting *ZT* in the *Pnma* phase for each compound is comparable to the highest value in the $Pm\bar{3}m$ phase shown in Fig. 10, which is, however, obtained for Ba_3PnN, where in reality the hexagonal phase is likely realized. In this sense, Ba_3GeO and Sr_3AsN with the *Pnma* phase are the most promising candidates investigated in this study. While there is a direction dependence of *ZT* to some extent for both compounds in the*Pnma* phase as shown in Fig. 16, the high *ZT* along all the directions is advantageous for technological applications.

IV. CONCLUSION

We investigate the thermoelectric performance of the hole-doped antiperovskite oxides and nitrides by means of first-principles band structure calculation and the subsequent transport calculation based on the Boltzmann transport theory. For the cubic $Pm\bar{3}m$ phase, we find that Ba_3PbO at low temperatures (around room temperature), Ca_3GeO at high temperatures, and Sr_3SbN in the wide temperature region are promising candidates for high

thermoelectric performance. In Ba_3PbO, multiple Dirac cones with sixfold degeneracy and the existence of the other valleys near the Γ and R points with relatively close energy levels enhance ZT. In Ca_3GeO and Sr_3SbN, quasi-one-dimensional band dispersion originating from the orbital anisotropy of the p orbitals is a key for their high performance. When considering the other crystal structures, the hexagonal structure is not favorable at least from the perspective of the shape of the band dispersion. However, the orthorhombic distortion toward the *Pnma* phase sizably enhances the thermoelectric performance of Ba_3GeO and Sr_3AsN, which are the most promising candidates within the materials investigated in this study. For both compounds, a crucial consequence of the structural distortion is the high valley degeneracy, which is considered to enhance their thermoelectric performance. For Ba_3GeO, another important role of the structural distortion is the gap opening. Another promising candidate is Ba_3AsN if synthesized as the *Pnma* phase, which is slightly unstable compared with the hexagonal phase in our calculation. Our study will help and stimulate the experimental exploration of the high thermoelectric performance in antiperovskite oxides and nitrides, which offer a unique and fertile playground where various kinds of characteristic electronic structure take place.

ACKNOWLEDGMENTS

Some calculations are performed using large-scale computer systems in the supercomputer center of the Institute for Solid State Physics, the University of Tokyo, and those of the Cybermedia Center, Osaka University. This study is supported by JSPS KAKENHI (Grants No. JP17H05481 and No. JP19H04697) and JST CREST (Grant No. JPMJCR16Q6), Japan.

APPENDIX: LIST OF THE OPTIMAL HOLE CARRIER DENSITY AT $T = 300$ K

The optimal hole carrier densities for ZT at $T = 300$ K are shown in Tables VI–X.

TABLE VI. Hole carrier density that maximizes the calculated ZT value, n_{opt}, at $T = 300$ K for oxides Ae_3TtO with the $Pm\bar{3}m$ phase.

Ae	*Tt*	n_{opt} (10^{20} cm^{-3})
Ca	Ge	0.5
	Sn	0.2
	Pb	0.1
Sr	Ge	0.4
	Sn	0.2
	Pb	0.1
Ba	Ge	6.8
	Sn	0.4
	Pb	0.5

TABLE VII. Hole carrier density that maximizes the calculated ZT value, n_{opt}, at $T = 300$ K for nitrides Ae_3PnN with the $Pm\bar{3}m$ phase.

Ae	*Pn*	n_{opt} (10^{20} cm^{-3})
Ca	As	0.6
	Sb	0.2
	Bi	0.1
Sr	As	0.9
	Sb	1.2
	Bi	0.2
Ba	As	4.0
	Sb	3.8
	Bi	4.3

TABLE VIII. Hole carrier density that maximizes the calculated ZT value, n_{opt}, at $T = 300$ K for materials with the $P6_3/mmc$ phase. In this table, n_{opt} for each axis is presented.

	n_{opt} (10^{20} cm^{-3})	
	$a = b$	c
Ba_3AsN	13	28
Ba_3SbN	0.7	22
Ba_3BiN	0.3	27

TABLE IX. Hole carrier density that maximizes the calculated ZT value, n_{opt}, at $T = 300$ K for materials with the *Imma* phase. In this table, n_{opt} for each axis is presented.

	n_{opt} (10^{20} cm^{-3})		
	a	b	c
Ca_3GeO	0.2	0.8	0.7
Ba_3SnO	0.2	0.2	0.2
Ba_3PbO	0.4	0.3	0.4

TABLE X. Hole carrier density that maximizes the calculated ZT value, n_{opt}, at $T = 300$ K for materials with the *Pnma* phase. In this table, n_{opt} for each axis is presented.

	n_{opt} (10^{20} cm^{-3})		
	a	b	c
Sr_3GeO	1.3	0.6	0.7
Ba_3GeO	1.7	1.6	1.5
Ca_3AsN	0.6	1.5	1.2
Sr_3AsN	2.5	2.2	3.0
Ba_3AsN	9.1	3.9	9.6

[1] H. J. Goldsmid, *Thermoelectric Refrigeration* (Plenum Press, New York, U.S.A., 1964).
[2] D. M. Rowe, *CRC Handbook of Thermoelectrics* (CRC Press, Boca Raton, U.S.A., 1995).

[3] B. Poudel, Q. Hao, Y. Ma, Y. Lan, A. Minnich, B. Yu, X. Yan, D. Wang, A. Muto, D. Vashaee, X. Chen, J. Liu, M. S. Dresselhaus, G. Chen, and Z. Ren, High-thermoelectric performance of nanostructured bismuth antimony telluride bulk alloys, Science **320**, 634 (2008).

[4] Z. H. Dughaish, Lead telluride as a thermoelectric material for thermoelectric power generation, Physica B **322**, 205 (2002).

[5] J. P. Heremans, V. Jovovic, E. S. Toberer, A. Saramat, K. Kurosaki, A. Charoenphakdee, S. Yamanaka, and G. J. Snyder, Enhancement of thermoelectric efficiency in PbTe by distortion of the electronic density of states, Science **321**, 554 (2008).

[6] J. Androulakis, I. Todorov, D. Y. Chung, S. Ballikaya, G. Wang, C. Uher, and M. Kanatzidis, Thermoelectric enhancement in PbTe with K or Na codoping from tuning the interaction of the light- and heavy-hole valence bands, Phys. Rev. B **82**, 115209 (2010).

[7] H. Wang, Y. Pei, A. D. LaLonde, and G. J. Snyder, Heavily doped p-type PbSe with high thermoelectric performance: An alternative for PbTe, Adv. Mater. **23**, 1366 (2011).

[8] W. Jeitschko and D. Braun, $LaFe_4P_{12}$ with filled $CoAs_3$-type structure and isotypic lanthanoid-transition metal polyphosphides, Acta Cryst. **B33**, 3401 (1977).

[9] D. T. Morelli, T. Caillat, J.-P. Fleurial, A. Borshchevsky, J. Vandersande, B. Chen, and C. Uher, Low-temperature transport properties of p-type CoSb, Phys. Rev. B **51**, 9622 (1995).

[10] G. S. Nolas, G. A. Slack, T. Caillat, and G. P. Meisner, Raman scattering study of antimony-based skutterudites, J. Appl. Phys. **79**, 2622 (1996).

[11] G. S. Nolas, G. A. Slack, D. T. Morelli, T. M. Tritt, and A. C. Ehrlich, The effect of rare-earth filling on the lattice thermal conductivity of skutterudites, J. Appl. Phys. **79**, 4002 (1996).

[12] B. C. Sales, D. Mandrus, and R. K. Williams, Filled skutterudite antimonides: A new class of thermoelectric materials, Science **272**, 1325 (1996).

[13] T. Takabatake, K. Suekuni, T. Nakayama, and E. Kaneshita, Phonon-glass electron-crystal thermoelectric clathrates: Experiments and theory, Rev. Mod. Phys. **86**, 669 (2014).

[14] I. Terasaki, Y. Sasago, and K. Uchinokura, Large thermoelectric power in $NaCo_2O_4$ single crystals, Phys. Rev. B **56**, R12685(R) (1997).

[15] V. Keppens, D. Mandrus, B. C. Sales, B. C. Chakoumakos, P. Dai, R. Coldea, M. B. Maple, D. A. Gajewski, E. J. Freeman, and S. Bennington, Localized vibrational modes in metallic solids, Nature **395**, 876 (1998).

[16] G. S. Nolas, J. L. Cohn, G. A. Slack, and S. B. Schujman, Semiconducting Ge clathrates: Promising candidates for thermoelectric applications, Appl. Phys. Lett. **73**, 178 (1998).

[17] B. C. Sales, B. C. Chakoumakos, R. Jin, J. R. Thompson, and D. Mandrus, Structural, magnetic, thermal, and transport properties of $X_8Ga_{16}Ge_{30}$ (X = Eu, Sr, Ba) single crystals, Phys. Rev. B **63**, 245113 (2001).

[18] C. H. Lee, I. Hase, H. Sugawara, H. Yoshizawa, and H. Sato, Low-lying optical phonon modes in the filled skutterudite $CeRu_4Sb_{12}$, J. Phys. Soc. Jpn. **75**, 123602 (2006).

[19] K. Suekuni, M. A. Avila, K. Umeo, and T. Takabatake, Cage-size control of guest vibration and thermal conductivity in $Sr_8Ga_{16}Si_{30-x}Ge_x$, Phys. Rev. B **75**, 195210 (2007).

[20] M. Christensen, A. B. Abrahamsen, N. B. Christensen, F. Juranyi, N. H. Andersen, K. Lefmann, J. Andreasson, C. R. H. Bahl, and B. B. Iversen, Avoided crossing of rattler modes in thermoelectric materials, Nat. Mater. **7**, 811 (2008).

[21] A. Fujiwara, K. Sugimoto, C.-H. Shih, H. Tanaka, J. Tang, Y. Tanabe, J. Xu, S. Heguri, K. Tanigaki, and M. Takata, Quantitative relation between structure and thermal conductivity in type-I clathrates $X_8Ga_{16}Ge_{30}$ (X = Sr, Ba) based on electrostatic-potential analysis, Phys. Rev. B **85**, 144305 (2012).

[22] M. Beekman, D. T. Morelli, and G. S. Nolas, Better thermoelectrics through glass-like crystals, Nat. Mater. **14**, 1182 (2015).

[23] T. Tadano, Y. Gohda, and S. Tsuneyuki, Impact of Rattlers on Thermal Conductivity of a Thermoelectric Clathrate: A First-Principles Study, Phys. Rev. Lett. **114**, 095501 (2015).

[24] T. Tadano and S. Tsuneyuki, Quartic Anharmonicity of Rattlers and its Effect on Lattice Thermal Conductivity of Clathrates from First Principles, Phys. Rev. Lett. **120**, 105901 (2018).

[25] Y. Pei, X. Shi, A. LaLonde, H. Wang, L. Chen, and G. J. Snyder, Convergence of electronic bands for high performance bulk thermoelectrics, Nature (London) **473**, 66 (2011).

[26] L. D. Hicks and M. S. Dresselhaus, Effect of quantum-well structures on the thermoelectric figure of merit, Phys. Rev. B **47**, 12727 (1993).

[27] L. D. Hicks and M. S. Dresselhaus, Thermoelectric figure of merit of a one-dimensional conductor, Phys. Rev. B **47**, 16631 (1993).

[28] H. Usui and K. Kuroki, Enhanced power factor and reduced Lorenz number in the Wiedemann–Franz law due to pudding mold type band structures, J. Appl. Phys. **121**, 165101 (2017).

[29] T. Yamamoto and H. Fukuyama, Possible high thermoelectric power in semiconducting carbon nanotubes ∼ A case study of doped one-dimensional semiconductors ∼, J. Phys. Soc. Jpn. **87**, 024707 (2018).

[30] A. I. Hochbaum, R. Chen, R. D. Delgado, W. Liang, E. C. Garnett, M. Najarian, A. Majumdar, and P. Yang, Enhanced thermoelectric performance of rough silicon nanowires, Nature (London) **451**, 163 (2008).

[31] R. S. Prasher, X. J. Hu, Y. Chalopin, N. Mingo, K. Lofgreen, S. Volz, F. Cleri, and P. Keblinski, Turning Carbon Nanotubes from Exceptional Heat Conductors Into Insulators, Phys. Rev. Lett. **102**, 105901 (2009).

[32] Y. Nakai, K. Honda, K. Yanagi, H. Kataura, T. Kato, T. Yamamoto, and Y. Maniwa, Giant Seebeck coefficient in semiconducting single-wall carbon nanotube film, Appl. Phys. Express **7**, 025103 (2014).

[33] K. Kuroki and R. Arita, "Pudding mold" band drives large thermopower in Na_xCoO_2, J. Phys. Soc. Jpn. **76**, 083707 (2007).

[34] K. Momma and F. Izumi, VESTA 3 for three-dimensional visualization of crystal, volumetric and morphology data, J. Appl. Crystallogr. **44**, 1272 (2011).

[35] T. He, Q. Huang, A. P. Ramirez, Y. Wang, K. A. Regan, N. Rogado, M. A. Hayward, M. K. Haas, J. S. Slusky, K. Inumara, H. W. Zandbergen, N. P. Ong, and R. J. Cava, Superconductivity in the non-oxide perovskite $MgCNi_3$, Nature **411**, 54 (2001).

[36] M. Oudah, A. Ikeda, J. N. Hausmann, S. Yonezawa, T. Fukumoto, S. Kobayashi, M. Sato, and Y. Maeno, Superconductivity in the antiperovskite Dirac-metal oxide $Sr_{3-x}SnO$, Nat. Commun. **7**, 13617 (2016).

[37] K. Takenaka and H. Takagi, Giant negative thermal expansion in Ge-doped anti-perovskite manganese nitrides, Appl. Phys. Lett. **87**, 261902 (2005).

[38] S. Iikubo, K. Kodama, K. Takenaka, H. Takagi, M. Takigawa, and S. Shamoto, Local Lattice Distortion in the Giant Negative Thermal Expansion Material $Mn_3Cu_{1-x}Ge_xN$, Phys. Rev. Lett. **101**, 205901 (2008).

[39] K. Kamishima, T. Goto, H. Nakagawa, N. Miura, M. Ohashi, N. Mori, T. Sasaki, and T. Kanomata, Giant magnetoresistance in the intermetallic compound Mn_3GaC, Phys. Rev. B **63**, 024426 (2000).

[40] K. Asano, K. Koyama, and K. Takenaka, Magnetostriction in Mn_3CuN, Appl. Phys. Lett. **92**, 161909 (2008).

[41] T. Tohei, H. Wada, and T. Kanomata, Negative magnetocaloric effect at the antiferromagnetic to ferromagnetic transition of Mn_3GaC, J. Appl. Phys. **94**, 1800 (2003).

[42] Y. Sun, X.-Qiu Chen, S. Yunoki, D. Li, and Y. Li, New Family of Three-Dimensional Topological Insulators with Antiperovskite Structure, Phys. Rev. Lett. **105**, 216406 (2010).

[43] T. Kariyado and M. Ogata, Three-dimensional Dirac electrons at the fermi energy in cubic inverse perovskites: Ca_3PbO and its family, J. Phys. Soc. Jpn. **80**, 083704 (2011).

[44] T. Kariyado and M. Ogata, Low-energy effective Hamiltonian and the surface states of Ca_3PbO, J. Phys. Soc. Jpn. **81**, 064701 (2012).

[45] T. H. Hsieh, J. Liu, and L. Fu, Topological crystalline insulators and Dirac octets in antiperovskites, Phys. Rev. B **90**, 081112(R) (2014).

[46] H. Kageyama, K. Hayashi, K. Maeda, J. P. Attfield, Z. Hiroi, J. M. Rondinelli, and K. R. Poeppelmeier, Expanding frontiers in materials chemistry and physics with multiple anions, Nat. Commun. **9**, 772 (2018).

[47] Y. Okamoto, A. Sakamaki, and T. Takenaka, Thermoelectric properties of antiperovskite calcium oxides Ca_3PbO and Ca_3SnO, J. Appl. Phys. **119**, 205106 (2016).

[48] K. Haddadi, A. Bouhemadou, L. Louail, F. Rahal, and S. Maabed, Prediction study of the structural, elastic and electronic properties of $ANSr_3$ (A = As, Sb and Bi), Comput. Mater. Sci. **46**, 881 (2009).

[49] K. Haddadi, A. Bouhemadou, L. Louail, S. Maabed, and D. Maouche, Structural and elastic properties under pressure effect of the cubic antiperovskite compounds $ANCa_3$ (A = P, As, Sb, and Bi), Phys. Lett. A **373**, 1777 (2009).

[50] K. Haddadi, A. Bouhemadou, and L. Louail, Structural, elastic and electronic properties of the hexagonal antiperovskites $SbNBa_3$ and $BiNBa_3$, Comput. Mater. Sci. **48**, 711 (2010).

[51] M. Bilal, Banaras Khan, H. A. Rahnamaye Aliabad, M. Maqbool, S. Jalai Asadabadi, and I. Ahmad, Thermoelectric properties of $SbNCa_3$ and $BiNCa_3$ for thermoelectric devices and alternative energy applications, Comput. Phys. Commun. **185**, 1394 (2014).

[52] M. Bilal, Saifullah, M. Shafiq, B. Khan, H. A. R. Aliabad, S. J. Asadabadi, R. Ahmad, and I. Ahmad, Antiperovskite compounds $SbNSr_3$ and $BiNSr_3$: Potential candidates for thermoelectric renewable energy generators, Phys. Lett. A **379**, 206 (2015).

[53] M. Hassan, I. Arshad, and Q. Mahmood, Computational study of electronic, optical and thermoelectric properties of X_3PbO (X = Ca, Sr, Ba) anti-perovskites, Semicond. Sci. Technol. **32**, 115002 (2017).

[54] M. Hassan, A. Shahid, and Q. Mahmood, Structural, electronic, optical and thermoelectric investigations of antiperovskites A_3SnO (A = Ca, Sr, Ba) using density functional theory, Solid State Commun. **270**, 92 (2018).

[55] J. Batool, S. Muhammad Alay-e-Abbas, and N. Amin, Thermodynamic, electronic, and magnetic properties of intrinsic vacancy defects in antiperovskite Ca_3SnO, J. Appl. Phys. **123**, 161516 (2018).

[56] E. Haque and M. A. Hossain, Enhanced thermoelectric performance in Ca-substituted Sr_3SnO, J. Phys. Chem. Solids **123**, 318 (2018).

[57] E. Haque and M. A. Hossain, Structural, elastic, optoelectronic and transport calculations of Sr_3SnO under pressure, Mater. Sci. Semicond. Process **83**, 192 (2018).

[58] E. Haque and M. A. Hossain, First-principles study of mechanical, thermodynamic, transport and superconducting properties of Sr_3SnO, J. Alloys Compd. **730**, 279 (2018).

[59] E. Haque, M. T. Rahman, and M. A. Hossain, Optoelectronic and thermoelectric properties of Ba_3DN (D = Sb, Bi): A DFT investigation, arXiv:1810.12526 (2018).

[60] E. Haque and M. A. Hossain, DFT based study on structural stability and transport properties of Sr_3AsN: A potential thermoelectric material, arXiv:1810.12531 (2018).

[61] B. Huang and J. D. Corbett, Orthorhombic inverse perovskitic Ba_3TtO (Tt = Ge, Si) as zintl phases, Z. Anorg. Allg. Chem. **624**, 1787 (1998).

[62] A. Velden and M. Jansen, Zur Kenntnis der inversen Perowskite M_3TO (M = Ca, Sr, Yb; T = Si, Ge, Sn, Pb), Z. Anorg. Allg. Chem. **630**, 234 (2004).

[63] J. Nuss, C. Mühle, K. Hayama, V. Abdolazimi, and H. Takagi, Tilting structures in inverse perovskites, M_3TtO (M = Ca, Sr, Ba, Eu; Tt = Si, Ge, Sn, Pb), Acta Cryst. **B71**, 300 (2015).

[64] F. Gäbler, M. Kirchner, W. Schnelle, U. Schwarz, M. Schmitt, H. Rosner, and R. Niewa, $(Sr_3N)E$ and $(Ba_3N)E$ (E = Sb, Bi): Synthesis, crystal structures, and physical properties, Z. Anorg. Allg. Chem. **630**, 2292 (2004).

[65] M. Y. Chern, D. A. Vennos, and F. J. Disalvo, Synthesis, structure, and properties of anti-perovskite nitrides Ca_3MN, M = P, As, Sb, Bi, Ge, Sn, and Pb, J. Solid. State Chem. **96**, 415 (1992).

[66] M. Y. Chern, F. J. Disalvo, J. B. Parise, and J. A. Goldstone, The structural distortion of the anti-perovskite nitride Ca_3AsN, J. Solid State Chem. **96**, 426 (1992).

[67] J. P. Perdew, A. Ruzsinszky, G. I. Csonka, O. A. Vydrov, G. E. Scuseria, L. A. Constantin, X. Zhou, and K. Burke,

Restoring the Density-Gradient Expansion for Exchange in Solids and Surfaces, Phys. Rev. Lett. **100**, 136406 (2008).

[68] G. Kresse and D. Joubert, From ultrasoft pseudopotentials to the projector augmented-wave method, Phys. Rev. B **59**, 1758 (1999).

[69] G. Kresse and J. Hafner, Ab initio molecular dynamics for liquid metals, Phys. Rev. B **47**, 558(R) (1993).

[70] G. Kresse and J. Hafner, Ab initio molecular-dynamics simulation of the liquid-metal-amorphous-semiconductor transition in germanium, Phys. Rev. B **49**, 14251 (1994).

[71] G. Kresse and J. Furthmüller, Efficiency of ab-initio total energy calculations for metals and semiconductors using a plane-wave basis set, Comput. Mater. Sci. **6**, 15 (1996).

[72] G. Kresse and J. Furthmüller, Efficient iterative schemes for ab initio total-energy calculations using a plane-wave basis set, Phys. Rev. B **54**, 11169 (1996).

[73] P. Blaha, K. Schwarz, G. K. H. Madsen, D. Kvasnicka, J. Luitz, R. Laskowski, F. Tran, and L. D. Marks, WIEN2k, *An Augmented Plane Wave + Local Orbitals Program for Calculating Crystal Properties* (Karlheinz Schwarz, Techn. Universität Wien, Austria, 2018). ISBN 3-9501031-1-2.

[74] A. D. Becke and E. R. Johnson, A simple effective potential for exchange, J. Chem. Phys. **124**, 221101 (2006).

[75] F. Tran and P. Blaha, Accurate Band Gaps of Semiconductors and Insulators with a Semilocal Exchange-Correlation Potential, Phys. Rev. Lett. **102**, 226401 (2009).

[76] N. Marzari and D. Vanderbilt, Maximally localized generalized Wannier functions for composite energy bands, Phys. Rev. B **56**, 12847 (1997).

[77] I. Souza, N. Marzari, and D. Vanderbilt, Maximally-localized Wannier functions for entangled energy bands, Phys. Rev. B **65**, 035109 (2001).

[78] J. Kuneš, R. Arita, P. Wissgott, A. Toschi, H. Ikeda, and K. Held, Wien2wannier: From linearized augmented plane waves to maximally localized Wannier functions, Comp. Phys. Commun. **181**, 1888 (2010).

[79] A. A. Mostofi, J. R. Yates, Y.-S. Lee, I. Souza, D. Vanderbilt, and N. Marzari, Wannier90: A tool for obtaining maximally-localised wannier functions, Comput. Phys. Commun. **178**, 685 (2008).

[80] Y. Obata, R. Yukawa, K. Horiba, H. Kumigashira, Y. Toda, S. Matsuishi, and H. Hosono, ARPES studies of the inverse perovskite Ca_3PbO: Experimental confirmation of a candidate 3D Dirac fermion system, Phys. Rev. B **96**, 155109 (2017).

[81] M. Ochi, H. Mori, D. Kato, H. Usui, and K. Kuroki, Thermoelectric performance of materials with $CuCh_4$ ($Ch = S, Se$) tetrahedra: Similarities and differences among their low-dimensional electronic structure from first principles, Phys. Rev. Mater. **2**, 085401 (2018).

[82] H. Mori, H. Usui, M. Ochi, and K. Kuroki, Temperature- and doping-dependent roles of valleys in the thermoelectric performance of SnSe: A first-principles study, Phys. Rev. B **96**, 085113 (2017).

[83] M. Ochi, H. Usui, and K. Kuroki, Prediction of the High Thermoelectric Performance of Pnictogen Dichalcogenide Layered Compounds with Quasi-One-Dimensional Gapped Dirac-like Band Dispersion, Phys. Rev. Appl. **8**, 064020 (2017).

[84] M. Ochi, H. Usui, and K. Kuroki, Theoretical aspects of the study on the thermoelectric properties of pnictogen-dichalcogenide layered compounds, J. Phys. Soc. Jpn. **88**, 041010 (2019).

[85] T. Yamamoto and H. Fukuyama, Bipolar thermoelectric effects in semiconducting carbon nanotubes: Description in terms of one-dimensional Dirac electrons, J. Phys. Soc. Jpn. **87**, 114710 (2018).

[86] A. Togo and I. Tanaka, First principles phonon calculations in materials science, Scr. Mater. **108**, 1 (2015).

[87] As a related study, a recent first-principles calculation [60] using the GGA-PBE functional [89] without SOC reported that Sr_3AsN with the $Pm\bar{3}m$ phase has no imaginary phonon frequency.

[88] T. Pandey, C. A. Polanco, V. R. Cooper, D. S. Parker, and L. Lindsay, Symmetry-driven phonon chirality and transport in one-dimensional and bulk Ba_3N-derived materials, Phys. Rev. B **98**, 241405(R) (2018).

[89] J. P. Perdew, K. Burke, and M. Ernzerhof, Generalized Gradient Approximation Made Simple, Phys. Rev. Lett. **77**, 3865 (1996).